INVITED FEATURE PAPER

Cation and vacancy disorder in $U_{1-y}Nd_yO_{2.00-x}$ alloys

Rozaliya I. Barabash[a)]
Materials Science and Technology Division, Oak Ridge National Laboratory, Oak Ridge, Tennessee 37831, USA

Stewart L. Voit
Fuel Cycle and Isotopes Division, Oak Ridge National Laboratory, Oak Ridge, Tennessee 37831, USA

Dilpuneet S. Aidhy
Department of Mechanical Engineering, University of Wyoming, Laramie, WY 82071, USA

Seung Min Lee and Travis W. Knight
Nuclear Engineering Department, College of Engineering and Computing, The University of South Carolina, Columbia, South Carolina 29208, USA

David J. Sprouster[b)] and Lynne E. Ecker
Nuclear Science and Technology Department, Brookhaven National Laboratory, Upton, New York 11973, USA

(Received 13 January 2015; accepted 10 August 2015)

In the present article, the intermixing and clustering of U/Nd, O, and vacancies were studied by both laboratory and synchrotron-based x-ray diffraction in $U_{1-y}Nd_yO_{2-x}$ alloys. It was found that an increased *holding time* at the high experimental temperature during initial alloy preparation results in a lower disorder of the Nd distribution in the alloys. Adjustment of the oxygen concentration in the $U_{1-y}Nd_yO_{2-x}$ alloys with different Nd concentrations was accompanied by the formation of vacancies on the oxygen sublattice and a nanocrystalline component. The lattice parameters in the $U_{1-y}Nd_yO_{2-x}$ alloys were also found to deviate significantly from Vegard's law when the Nd concentration was high (53%) and decreased with increasing oxygen concentration. Such changes indicate the formation of large vacancy concentrations during oxygen adjustment at these high temperatures. The change in the vacancy concentration after the oxygen adjustment was estimated relative to Nd concentration and oxygen stoichiometry.

I. INTRODUCTION

Interest in actinide and lanthanide chemistry reflects the growing demand for nuclear energy and nuclear fuel reprocessing.[1,2] Understanding the thermodynamics, structure, and reaction mechanisms between rare earth (RE) elements and actinides is required to predict the behavior of uranium oxides as a nuclear fuel sources.[3–6] In addition, studies on different actinide separation schemes are vital to reprocessing efforts of nuclear waste in the US and other countries.[2,7] For the safe disposal of nuclear waste, knowledge of the basic system chemistry is also needed to predict radio nuclei escape from multi-barrier repository systems and subsequent contamination of the environment.[8]

Both the structure and electronic properties of the cations have been shown to play a very important role in the behavior of nuclear fuel. Theoretical chemistry and x-ray absorption near edge spectroscopy (XANES) have been used for the characterization of actinide–ligand bonds especially their frontier orbitals.[9,10] The valence state for uranium, specifically, the formal 2*p*-6*d* transition was probed by XANES multiedge experiments by several authors because of its convenient energy −17.2 keV.[10] These studies focused on the change in the ionic radius of the cations.[11,12] Furthermore, several RE elements are high-yield fission products in UO_2 nuclear fuel and they readily dissolve in the fluorite crystal structure ($Fm\bar{3}m$). The cations are largely immobile, compared to oxygen in the crystal lattice of an (A, B)$O_{2\pm x}$ mixed oxide. A completely disordered (U, RE)$O_{2\pm x}$ may however transit to include some short-range ordering depending on exact thermodynamics.

Previously, it was found that solid solutions are easily formed between UO_2 and REs oxides.[13] The lattice parameter change of the $U_{1-y}RE_yO_{2.00-x}$ solid solutions with stoichiometry led to the discussion of the role of oxygen vacancies in these materials.[13] The heat capacity and thermodynamic properties of the initial oxides can be found in Ref. 14 for Nd_2O_3, and in Refs. 15–19 for the UO_2 and UO_2-based oxides.[20–23] The coordination model for the defect structure in hyperstoichiometric UO_{2+x} was described in the Refs. 7 and 24. Recently, a new approach to model nuclear oxides in the environment was

Contributing Editor: Yang-T. Cheng
Address all correspondence to these authors.
[a)]e-mail: rbarabas@utk.edu
[b)]e-mail: dsprouster@bnl.gov
This paper has been selected as an Invited Feature Paper.
DOI: 10.1557/jmr.2015.261

https://doi.org/10.1557/jmr.2015.261 Published online by Cambridge University Press

suggested assuming the existence of the miscibility gap at low temperature (<750 K) in the U–Nd–O phase diagram.[25] Desgranges et al.[25] argue that the formation of the miscibility gap may result in a competition between oxygen vacancy and U^{5+} cation formation to maintain the electroneutrality in (U, Nd)$O_{2\pm x}$.

This model motivates our further experimental investigation of cation disorder in $U_{1-y}R_yO_{2.00-x}$ solid solutions. In this work, x-ray diffuse and diffraction methods are used to reveal information on the defect structure of aliovalent cation species in (U, Nd)$O_{2\pm x}$. The goal of this work is to generate data to verify the chemical thermodynamic models of nuclear fuel used in the coupled meso- and continuum-scale fuel performance models under normal operating and accident conditions.

II. EXPERIMENTAL PROCEDURES

A. Samples preparation

Four groups of samples with the following Nd concentrations were studied: Group A-5.6 at.%; group B-15.5 at.%; group C-29.5 at.%; and group D-53 at.% (Table I). A more detailed description of sample preparation can be found elsewhere,[26] and we briefly describe the preparation conditions here. Each sample was pressed into a pellet at 280 MPa for 5 min. After pressing, the pellets were heated at 450 °C for 5 h to evaporate any residual moisture and then sintered in 4% H_2–96% Ar mixture gas for 5 h at 1600 °C to form consolidated pellets.

The pellets were oxidized or reduced in the thermogravimetric analyzer (NETZSCH STA409 Simultaneous thermal analysis, Selb, Germany) to produce different O/M ratio by using different hydrogen gas mixtures at the experimental temperatures summarized in the Table I. Next, the pellets were ground using a mortar and pestle for the x-ray diffraction (XRD) test. The particle size of the ground powder was less than 50 μm [confirmed by transmission electron microscopy (TEM)]. Each sample described in Table I was sealed well after fabrication and kept being sealed until XRD test, to limit exposure to air. XRD measurements were performed at room temperature. Furthermore, the samples do not oxidize during the XRD measurements as UO_2 is reasonably stable in the atmosphere at room temperature, and the measurements are rapid.

A co-conversion process was used to synthesize (U, Nd)$O_{2\pm x}$ reference materials for the thermochemical measurements. The metal elements were dissolved in a solution of dilute nitric acid and ammonium nitrate. The inorganic salt solution was fed into a heated rotary kiln where it decomposes and forms an ammonium nitrate–metal nitrate double salt: $(NH_4)_zMO_z(NO_3)_4{\cdot}zH_2O$ (M denotes the metals U and Nd).

Decomposition occurs in three distinct steps: (i) dehydration of the ammonium nitrate–metal nitrate–hydrate double salt forms a tetranitrate, (ii) decomposition of the anhydrous tetranitrate, without melting, at 170–270 °C forms a trinitrate salt, (iii) decomposition of the trinitrate, without melting, at 270–300 °C yields an intimate mixture of amorphous UO_3 and Nd_2O_3. Subsequent heating to >500 °C under a controlled partial pressure of oxygen causes reduction to (U, Nd)$O_{2\pm x}$ and crystallization of nanosized grains (see Fig. 1). Thermal treatment of the (U, Nd)$O_{2\pm x}$ powder at high temperatures produces a single fluorite phase solid solution. Samples for XRD analysis were prepared in a furnace under varied conditions of time, temperature, and oxygen potential to achieve the desired oxygen to metal ratios.

TABLE I. Oxidation conditions for $U_{1-y}Nd_yO_{2-x}$.

Nd (at. %)	O/M ratio	Pellet no.	Pellet press (MPa)	Heat treat. (°C)	Exp. temp. (°C)	Holding time (h)	pO_2 (atm)
DUO_2	O/U: 2.0	...	280	1600	1000	5	4.02×10^{-24}
5.60	O/M: 2.0	A1	280	1600	1000	6	8.59×10^{-16}
5.60	O/M: 1.9971	A2-1	280	1600	1300	5	4.38×10^{-15}
5.60	O/M: 2.0162	A2-2	280	1600	1300	5	2.07×10^{-06}
5.60	O/M: 2.0690	A2-3	280	1600	1000	5	6.50×10^{-01}
15.50	O/M: 2.0	B1	280	1600	1000	10	2.64×10^{-13}
15.50	O/M: 1.996	B2	280	1600	1000	10	8.54×10^{-18}
15.50	O/M: 1.9932	B3	280	1600	1300	7	1.52×10^{-12}
15.50	O/M: 1.9908	B4-1	280	1600	1300	7	7.72×10^{-04}
15.50	O/M: 1.9858	B4-2	280	1600	1300	7	8.60×10^{-15}
15.50	O/M: 2.1556	B5	280	1600	1000	7	6.50×10^{-01}
29.50	O/M: 1.9934	C1	280	1600	1000	7	7.49×10^{-15}
29.50	O/M: 2.0	C2	280	1600	1000	7	9.02×10^{-12}
29.50	O/M: 1.9840	C3	280	1600	1000	7	8.40×10^{-17}
29.50	O/M: 1.9737	C4-1	280	1600	1300	7	1.35×10^{-12}
29.50	O/M: 2.0789	C4-2	280	1600	1000	7	6.50×10^{-01}
53	O/M: 2.0	D1	280	1600	1000	7	6.50×10^{-01}
53	O/M: 1.9023	D2-1	280	1600	1000	7	6.01×10^{-17}
53	O/M: 1.8906	D2-2	280	1600	1000	7	1.37×10^{-17}

https://doi.org/10.1557/jmr.2015.261 Published online by Cambridge University Press

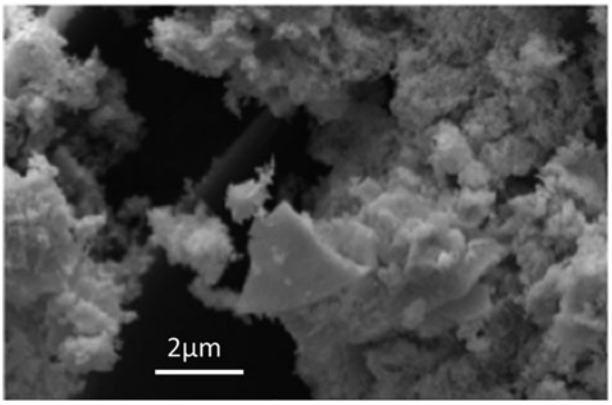


FIG. 1. Fully reduced $U_{84.5}Nd_{15.5}O_2$ powder.

Parameters of sample preparation (holding time and temperature for different U:Nd:O ratio) are summarized in Table I. A second group of four samples with O/M = 2 were prepared under the same conditions described above for synchrotron measurements with equal holding time for all samples.

B. Kinetics of oxygen adjustment

Oxygen adjustment may also cause some oxygen atoms to form a new layer at the surface of the crystal and diffuse into the material. Therefore, the oxygen adjustment kinetics in the $U_{1-y}Nd_yO_{2-x}$ alloys is controlled by the diffusion processes of the oxygen and vacancies in the material. The holding time during adjustment should allow the oxygen and vacancies to penetrate through half of the sample, assuming that diffusion occurs from both surfaces of the pellet. The time, τ, for one dimensional diffusion can be roughly estimated from the equation: $\langle x^2 \rangle = 2D\tau$, where D is the diffusion coefficient at the adjustment temperature, $\langle x^2 \rangle$ is the mean square displacement of the oxygen anions or vacancies, and x is the mean depth from the surface of the pellet to the middle of the sample. Moreover to provide the equilibrium homogeneous oxygen distribution across the sample, the holding time should be further increased. Therefore, the holding time should be corrected for oxygen anions and vacancies to not only reach the midst of the sample but also to become homogeneous across the sample and for Nd/U cations to adjust to the change in oxygen vacancy concentration change. Experimentally, this time was determined by controlling the sample weight and giving enough time for weight value to saturate.

C. Diffraction measurements

Firstly, all samples were characterized by laboratory XRD measurements in reflection geometry using Rigaku diffractometer (Cu K_α x-rays). The second set of samples with O/M ratios equal to 2 was further studied with high-resolution XRD (HRXRD) and pair distribution function (PDF) analysis. HRXRD and PDF measurements were performed at the National Synchrotron Light Source, using beamline X17A. All synchrotron measurements were performed in transmission geometry with an amorphous silicon-based flat panel detector (Perken-Elmer) mounted orthogonal to the beam path and centered on the beam. The sample-to-detector distances and tilts of the detector relative to the beam were refined using a Nickel powder standard. The wave length of the incident x-rays was 0.1859 Å (66.66 keV). The sample-to-detector distance was calculated to be ~208 mm (PDF) and 411 mm (XRD). Multiple patterns were collected on 16 different regions of each sample. The count time was adjusted to ensure maximum signal and minimize over-saturation of the detector (0.1 s for all samples) and each individual pattern consisted of 100 individual exposures. The two-dimensional images were then averaged together and radially integrated, to obtain the one-dimensional diffraction patterns. The scattering component from the kapton/air component was subtracted prior to the XRD analysis. The diffraction patterns collected with the PDF set-up were background corrected, normalized, and converted to atomic PDFs, G(r), over a Q-range of 1–25 $Å^{-1}$. The XRD patterns were refined with the TOPAS (Bruker) software package. Two separate analysis procedures were performed on the synchrotron data sets. The first was a simple peak profile fitting procedure, where the full width at half maximum (FWHM) for nonoverlapping peaks was determined.

The second was a traditional two phase Rietveld refinement. For both analyses, the peak profiles were modeled by a modified Thompson–Cox–Hastings pseudo-Voigt profile function. For the Rietveld refinements, the instrument contribution to the broadening of the measured profiles was quantified by fitting a Ni NIST powder standard, with known crystalline-domain size and negligible strain contribution. The Gaussian and Lorentzian-based broadening parameters were subsequently fixed during the analysis of the samples under investigation. The patterns were refined assuming a two phase mixture of bulk UO_2 with Nd atoms substitutionally located on the U sites and a nanophase of Nd:UO_2. The lattice parameters, weight fraction, and domain size of the nanophase clusters were allowed to refine during the Rietveld refinements with the temperature factors nominally fixed to their bulk values taken from the literature.[27] The O, U, and Nd site occupancies in the bulk UO_2 matrix were allowed to vary during the fitting with the sum of the U and Nd atoms restrained to equal unity (U + Nd = 1). The occupancies of the U and Nd atoms in the nanophase were set to the respective stoichiometric values, with their sum equal to unity (U + Nd = 1). Allowing the occupancies of the U, Nd, and O atoms in the nanophase to refine resulted in poor fits and nonphysical parameters.

https://doi.org/10.1557/jmr.2015.261 Published online by Cambridge University Press

III. RESULTS AND DISCUSSION

A. Analysis of the FWHM

A typical XRD diffraction pattern collected from a group A sample is shown in Fig. 2. Enlarged peak profiles for several orders of (*h*00) type reflections are shown in Fig. 3 for samples A1, C1, and C3. The shape of the profiles of individual peaks (Fig. 4) reveals that a diffuse-scattering component is observed for all studied alloys. It is evident from the large changes in FWHM and the complicated shape of the intensity maxima (which sometimes split into several subpeaks), that in the A and C samples, the cation disorder is high before the oxygen adjustment. The overall FWHM for all studied samples is shown in Fig. 4 as a function of the Miller indices of the reflection:

$$\sqrt{h_i^2} = \sqrt{h^2 + k^2 + l^2} \quad .$$

The analysis of the FWHM as a function of Miller indices (*hkl*) indicates that the FWHM does not monotonically increase with (*hkl*) as is expected for a single phase material without defects (Fig. 4). Instead highly anisotropic behavior is found which is consistent with regions (or clusters) with relatively high short-range order surrounded by a disordered region. In the first set of A, B, C, D samples with varying initial holding time, the smallest FWHM is observed for sample with higher initial holding time (group D), and the largest for A samples with the smallest holding time (Fig. 4). An increase of the FWHM correlates with structural heterogeneity and Nd cation disorder in the material.

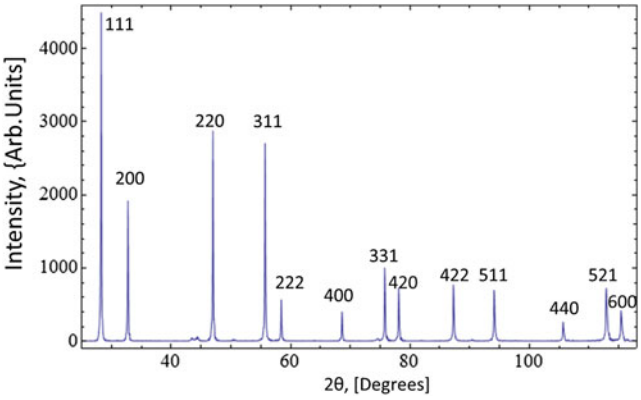


FIG. 2. A typical diffraction pattern from sample (U + 5.6% Nd)O_2.

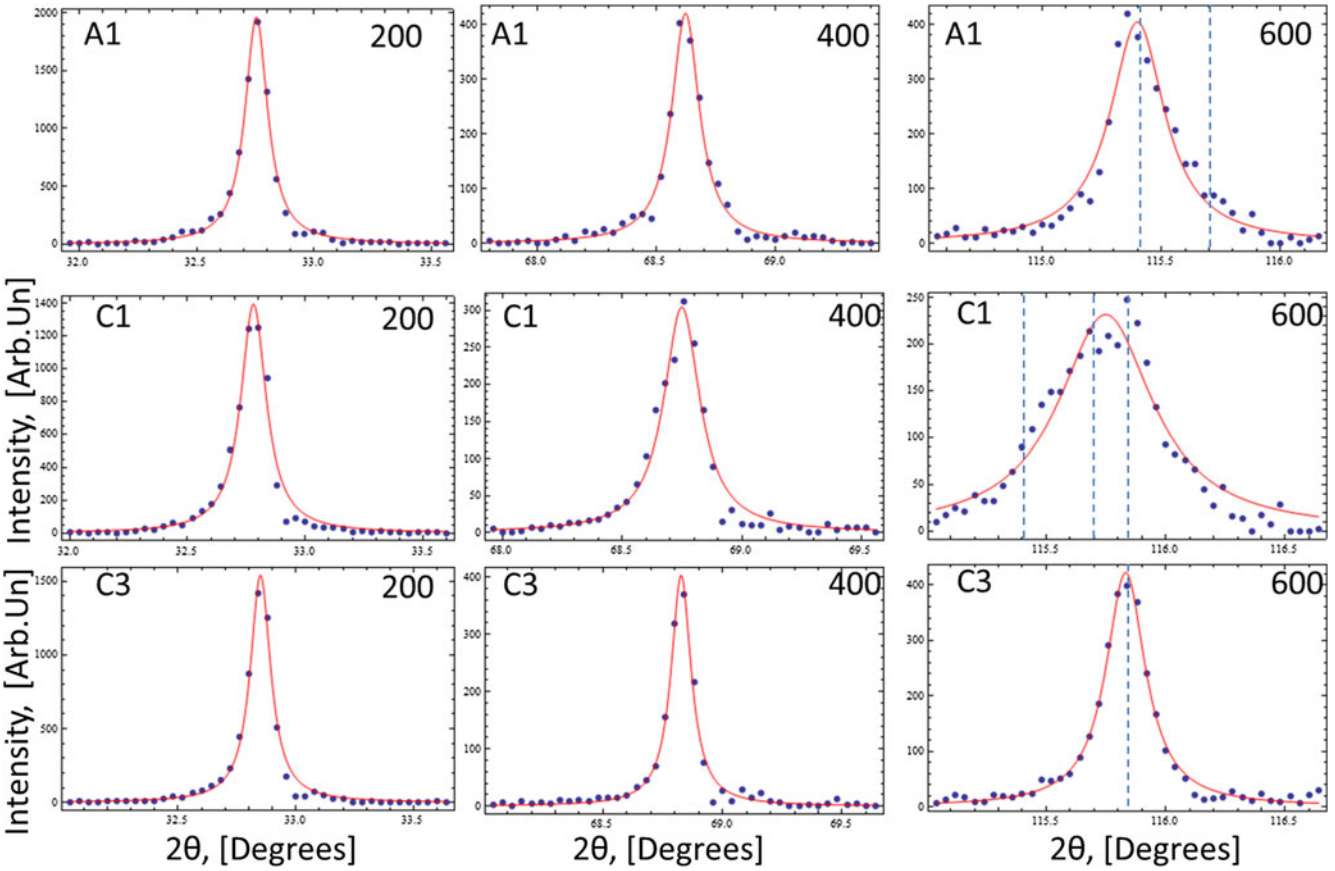


FIG. 3. Peak profiles for several orders of (*h*00) type reflections for group A and C. Dashed lines for (600) profiles mark the positions of the subpeaks and peak displacement.

https://doi.org/10.1557/jmr.2015.261 Published online by Cambridge University Press

The reason for the higher structural disorder in samples from group A probably relates to insufficient holding time during the initial oxidation conditions (compare Table I) causing a heterogeneous distribution of Nd cations across the sample. Cation disorder does not vary significantly for sample group B which was subjected to longer initial holding time. This demonstrates that increasing the holding time improves the homogeneity of the Nd cations across the sample.

Samples prepared with equal initial holding times studied with synchrotron HRXRD show a systematic increase in the FWHM with the increasing Nd content (Fig. 5). This indicates that structural disorder increases with increasing Nd concentration in the alloy.

Figures 4 and 5 both show that there is an anisotropic broadening in the FWHM in the different *hkl* families, with more broadening along particular *hkl* directions, consistent with previous literature.[28–30] This behavior is typical for small clusters of ordered regions in a disordered matrix. The possibility of the coherent clusters formation agrees with earlier models.[2,5,7,24,30]

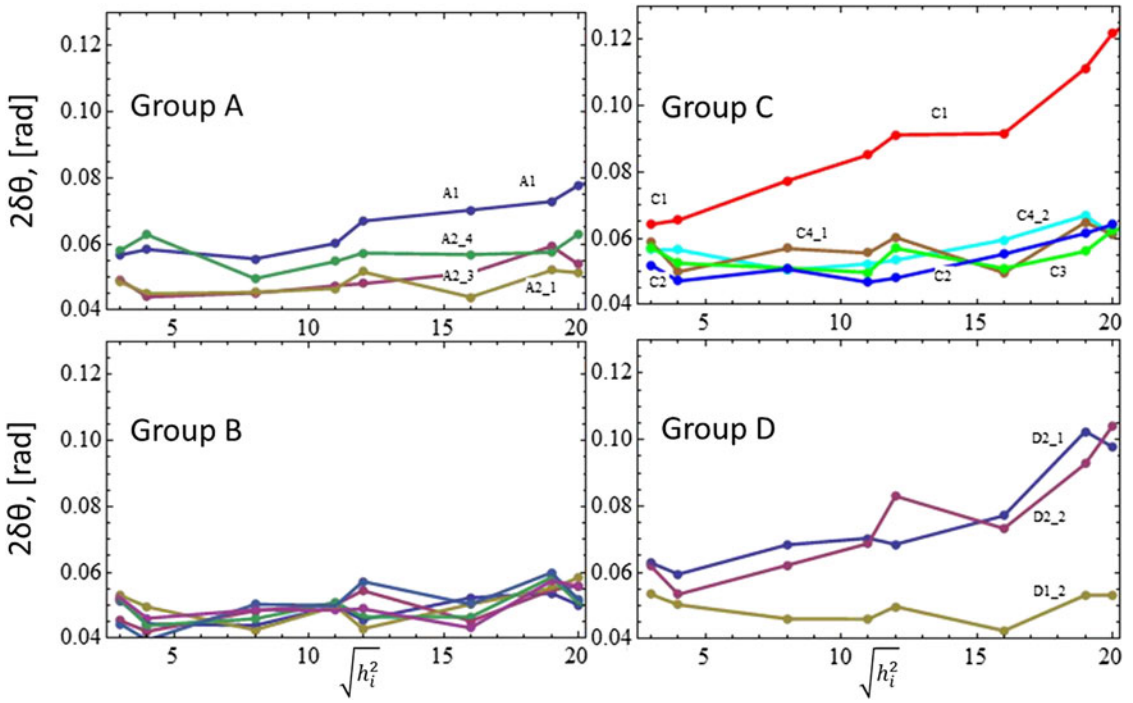


FIG. 4. FWHM for A, B, C, and D groups of sample for first 8 (*hkl*) peaks. Positions of the different (*hkl*) peaks are marked with dashed vertical lines. Left bottom frame indicates the (*hkl*) of the lines for convenience.

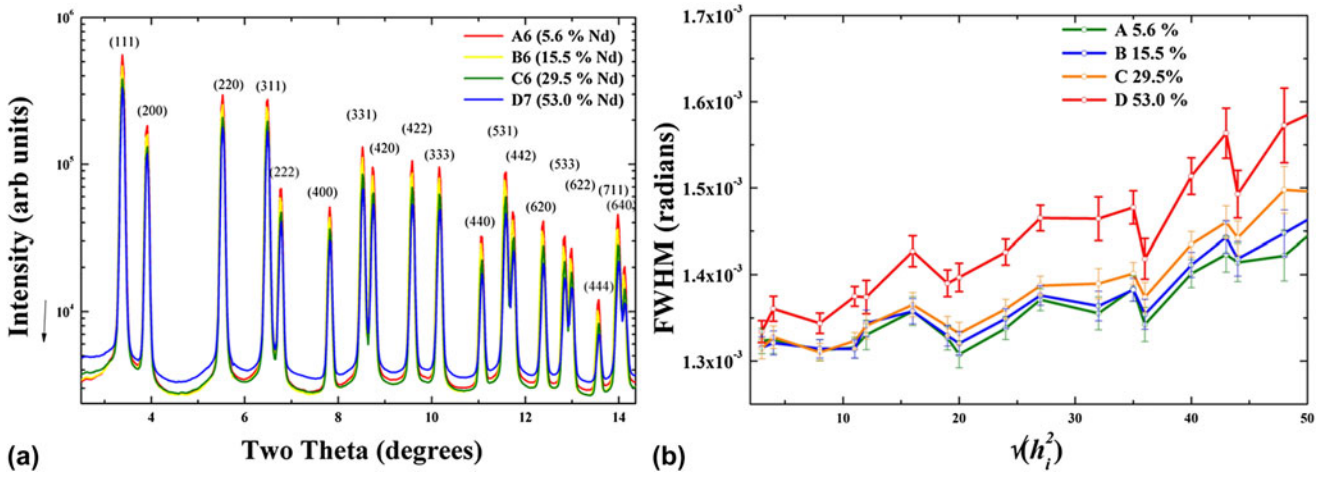


FIG. 5. (a) HRXRD patterns for the UNdO A, B, C, and D samples for O/M = 2; (b) FWHM calculated from the synchrotron measurements at oxygen concentration equal to 2.0 for A, B, C and D samples prepared at equal initial holding time for all samples.

https://doi.org/10.1557/jmr.2015.261 Published online by Cambridge University Press

B. Size mismatch

Relative differences between the interatomic *d*-spacings of UO_2 and $U_{1-y}Nd_yO_{2-x}$ consistently increase with Nd concentration from sample group A to D (Fig. 6). The lattice parameter of the $U_{1-y}Nd_yO_{2-x}$ alloys consistently decreases with increasing Nd concentration at M/O = 2 (Fig. 7). The atomic radius of a U atom is smaller than a Nd atom.[31] In the crystal lattice of each dioxide, and in the $U_{1-y}Nd_yO_{2-x}$ alloy, the atoms can occupy two different sublattices: (*) U/Nd sublattice or (**) oxygen sublattice [Fig. 8(a)]. Larger Nd or U atoms occupy the corners and face centers in the cubic unit cell, while oxygen atoms are arranged in the centers of 8 cublets. The unit cell can thus be split into 8 subcells with an oxygen atom in the center. These two sublattices are not equivalent and they provide a coordination 4:8 in the $U_{1-y}Nd_yO_{2-x}$ structure. This way at the U/Nd sublattice each atom is surrounded by 8 oxygen atoms, while at the oxygen sublattice each lattice site is in the center of a tetrahedron formed by U/Nd atoms. Moreover, the $U_{1-y}Nd_yO_{2-x}$ compound is an ionic crystal with U/Nd ions bearing the "+", and oxygen ions bearing the "–" charge.

When Nd atoms are added to the UO_2 to form $U_{1-y}Nd_yO_2$ alloys, the Nd atoms can substitute some of the U atoms at the U/Nd sublattice. The Nd has a 3+ charge state and will be sitting on a U 4+ state. Therefore, charge balancing defects are required in the form of U5+ smaller cations or oxygen vacancies. While oxygen ions are typically larger than the U5+ ions, the lattice relaxation around the oxygen vacancy causes it to be smaller than the substituted oxygen ion (see Sec. III. C). As such, both U5+ ions and oxygen vacancies can potentially cause a contraction in the lattice parameter.

Nd 3+ ions have a larger size than U4+ and U5+ ions ($\Delta V > 0$). An Nd ion has a radius of 0.983 Å, while U5+ and U4+ ions have Shannon radii of 0.76 and 0.89 Å (respectively). Adding an U5+ and an Nd3+ radii together leads to an overall average change in radius of −0.02 per Nd3+ ion. This is almost 2.5x larger than the observed contraction in the lattice parameter (Fig. 7). This is an indication that the change in charge, from U4+ to U5+, is not the sole cause of the contraction in the lattice parameter, and that there should be an interplay with another mechanism resulting in the observed contraction of the lattice parameter. Due to the size mismatch

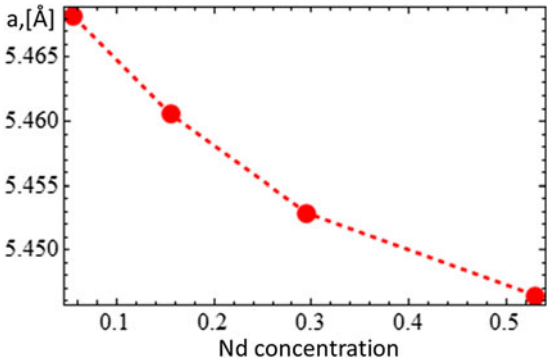


FIG. 7. Dependence of lattice parameter on Nd concentration for oxygen concentration equal 2.0.

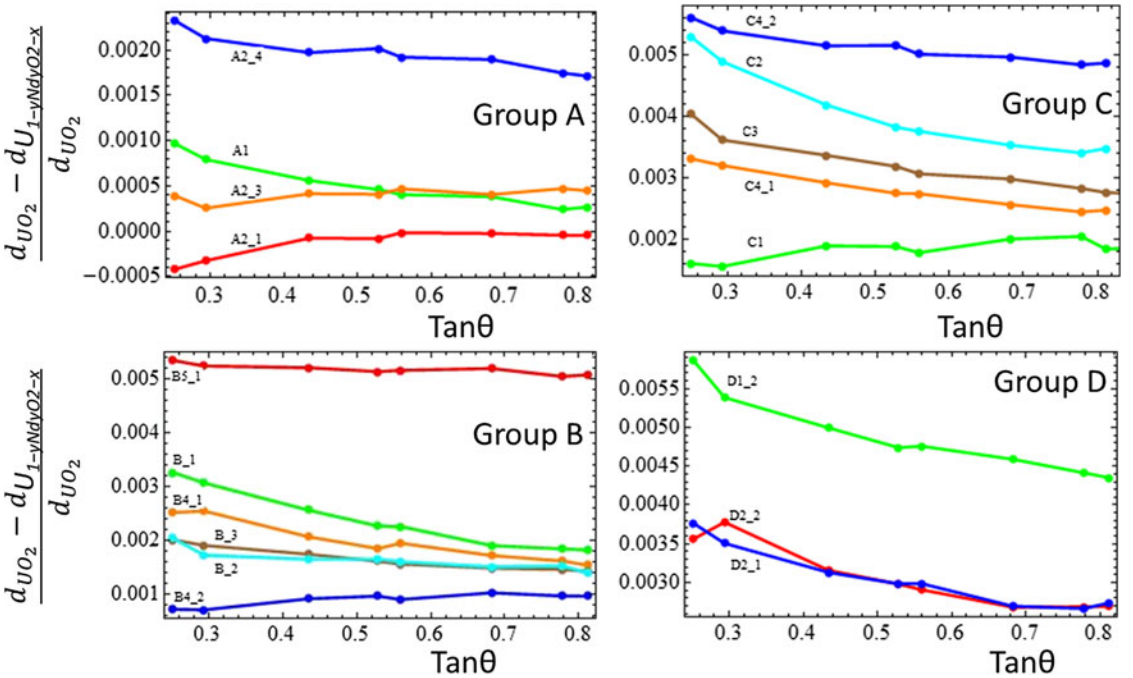


FIG. 6. Relative difference between the lattice parameter of $U_{1-y}Nd_yO_{2-x}$ and UO_2 for A, B, C, and D groups of samples.

https://doi.org/10.1557/jmr.2015.261 Published online by Cambridge University Press

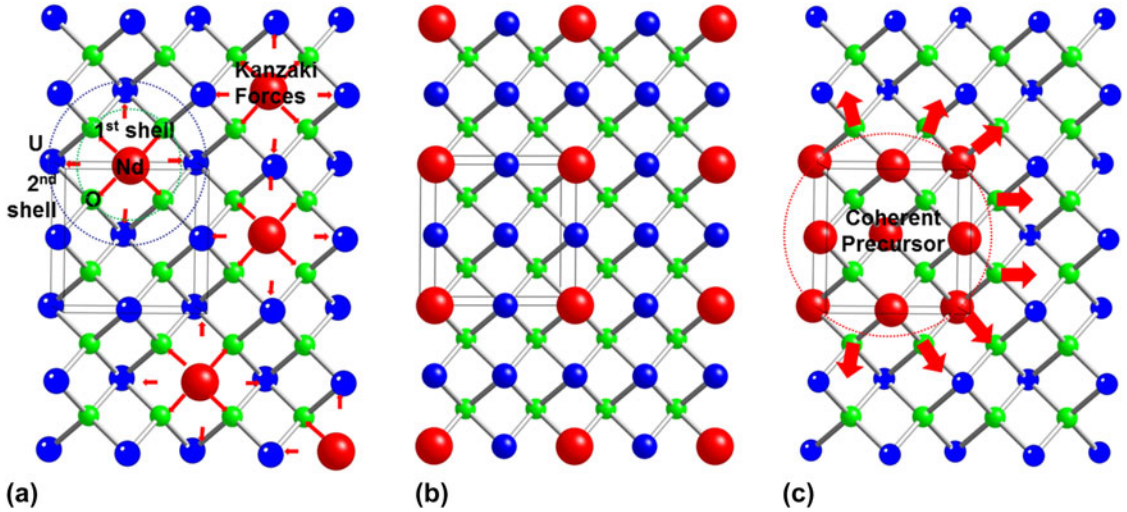


FIG. 8. (a) Random distribution of Nd atoms at the U sublattice. Larger Nd atoms (red) locally expand the lattice and "push" the near-neighbor oxygen atoms (green) forming the first neighbor shell and U atoms (blue) forming the second shell surrounding Nd atoms. Nd atoms create large distortions in the lattice, which are described with Kanzaki forces indicated by red arrows. (b) Fully ordered arrangement of Nd and U atoms at the U/Nd sublattice. (c) Early stages of phase separation result in the formation of the cluster or coherent precursor of the second phase in the UO_2 matrix. A quarter of the layer is used in the out of plane direction and the unit cell is marked at all frames for convenience.

between the Nd and U ions, the larger Nd atoms push the neighboring ions out of their regular positions, forming the so-called "Kanzaki forces".[32–36] This will essentially create static displacements,[37–39] lattice distortions, and increase the energy of the crystal [Fig. 8 (a)]. The completely random distribution of Nd atoms on the U/Nd sublattice is shown in Fig. 8(a). Depending on the parameters of the elastic interactions, the atomic arrangements in the solid solution can differ ranging from a fully ordered distribution of Nd and U atoms at the U/Nd sublattice [Fig. 8(b)], to early stages of phase separation with the formation of the coherent Nd-rich clusters [Fig. 8(c)] creating much larger distortions at the cluster/matrix interface. This supports the recently reported existence of the miscibility gap in the U–Nd–O phase equilibrium diagram and co-existence of the two phases.[25] The static distortions around the clusters, as well as vacancies, can also cause attenuation of the Bragg reflections and relate to the so-called "static Debye–Waller factor" (DWF). The attenuation of the peaks with different (*hkl*) values due to static DWF should increase with Miller indices of the reflection, h_i, as $\sqrt{h_i^2}$ of the reflection. The intensity, I, lost from the attenuated Bragg peaks appears as diffuse Huang scattering $I_H \sim 1/\boldsymbol{q}^2$ in the vicinity of each Bragg peak. Here, $\boldsymbol{q} = \boldsymbol{Q} - \boldsymbol{G}$, where $\boldsymbol{Q}$ is the momentum transfer, and $\boldsymbol{G}$ is the nearest to $\boldsymbol{Q}$ reciprocal lattice vector. This decrease in scattering intensity is clearly visible in Fig. 5(a), with the addition of a diffuse-scattering component that increases with increasing Nd concentration. Different stoichiometries of the cubic Nd–U–O can be also formed with the addition of Nd atoms, such as $NdU_3O_{9.51}$; $Nd_{1.4}U_{2.6}O_{9.04}$; $Nd_{1.99}U_{2.01}O_{8.35}$; $Nd_{2.4}U_{1.6}O_{7.87}$; $Nd_{2.81}U_{1.19}O_{7.39}$; $Nd_3UO_{7.17}$ with the corresponding lattice parameters 5.412; 5.416; 5.423; 5.426; 5.447; 5.448 Å,[40] although both XRD and HRXRD results given here do not identify such individual phases.

C. Vacancies

Vacancies are always present in certain concentrations in crystals at thermal equilibrium.[41] For example, the equilibrium concentration of individual vacancies with temperature, T, follows the equation[42]:

$$c_v = \mathrm{Exp}\frac{\Delta S_v}{k_B}\mathrm{Exp}\left(-\frac{\Delta H_v}{k_B T}\right) \quad ,$$

where ΔS_v, ΔH_v, are the entropy and enthalpy of vacancy formation, and k_B is Boltzman constant.

Vacancy formation increases the configurational entropy as vacancies can occupy any lattice site. Therefore, they are thermodynamically favorable despite an increase in the energy of the system.

The larger substitutional Nd atoms should typically expand the lattice leading to a larger lattice parameter. The experimental data shown here, however, display the opposite trend. As mentioned in the previous section, the formation of vacancies is one of the possible causes of the lattice contraction. The distortion fields surrounding the Nd atoms can be partially relaxed and elastic energy related to these distortions can be partially decreased if a vacancy will approach the larger Nd atom (Fig. 9) because the distortion fields from the larger Nd atom and from the vacancy partially compensate each other.

https://doi.org/10.1557/jmr.2015.261 Published online by Cambridge University Press

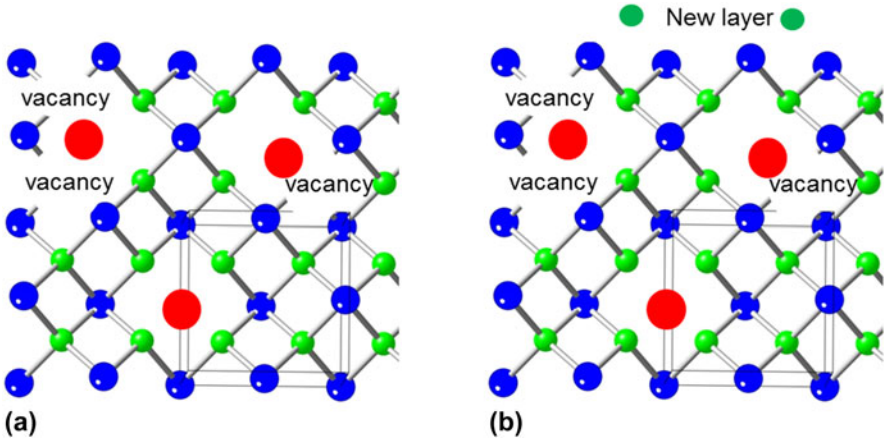


FIG. 9. (a) Formation of vacancy or bi-vacancy near the Nd atom creates an "extra" space and allows the lattice to accommodate the larger substitutional Nd atom with much lower distortions. (b) Formation of the new layer of the material during oxygen adjustment.

Therefore, the probability of vacancy formation near the Nd atoms is much larger than near the U atoms. It may happen that a gain in the resulting elastic energy is even larger if two or more vacancies form near the Nd atom [Fig. 9(a)]. One possible explanation for this opposite trend is the non-negligible role of vacancies in the $U_{1-y}Nd_yO_{2-x}$ substitutional solid solution. This possibility was also suggested by Ohmichi et al.[13] The formation of oxygen vacancies in $U_{1-y}Nd_yO_{2-x}$ may cause U and Nd cations to change their charge state. Sickafus et al.[7] have previously shown that to obtain an oxygen–deficient fluorite structure, the 4+ cations should be replaced by aliovalent cations with (3+, 2+, and 1+) charges. To keep the electroneutrality of the material, this should be accompanied by the formation of oxygen vacancies. For the $U_{1-y}Nd_yO_{2-x}$, samples discussed here the formation of pyrochlore type ($U_2Nd_2O_7$) complexes in the solid solution[13,43] may take place. Uncompensated local deviation from electroneutrality gives rise to charge density waves, which were observed in UO_2 and similar materials.[44–46] Charge density waves influence the anharmonicity, thermal conductivity, and phonon lifetime, which are of great importance for the performance of these materials.[47]

D. Oxygen adjustment

The oxygen concentration adjustment also modifies the lattice parameters within each group of samples (Figs. 6 and 10). Lattice parameters and *d*-spacings also consistently decrease with oxygen concentration at all Nd concentrations, which agrees with previous observations by Ohmichi et al.[13]

For samples with oxygen concentrations equal to 2.0, (O/M = 2) (i.e., stoichiometric $U_{1-y}Nd_yO_2$) the lattice parameter dependence on the Nd concentration deviates from linearity for concentration of Nd approaching 50%. This is shown in Fig. 7 and demonstrates that the alloys

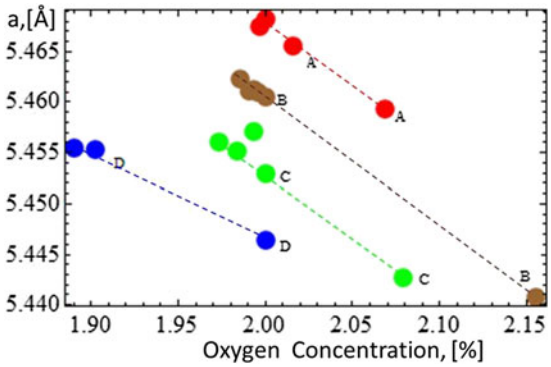


FIG. 10. Dependence of lattice parameter on oxygen and Nd concentration. Red—5.6%; Brown—15.5%; Green—29.5%; Blue—53%. Dashed lines are guides for eye.

do not exactly follow Vegard's law for highly concentrated solutions. The dependence of lattice parameter on both Nd and oxygen concentration for all groups of alloys is shown in Fig. 10. The lattice parameters and *d*-spacings consistently decrease with oxygen concentration at all Nd concentrations. For all sample groups, the contraction lattice parameter decreases with the increasing oxygen concentration. This behavior is again highly correlated to the formation of vacancies during oxygen adjustment. During oxygen adjustment, the alloy must remain neutral; otherwise, the electrostatic interaction energy will be too high. This implies that the numbers of vacancies formed at the oxygen sublattice and U/Nd sublattice [Figs. 11(b) and 11(c)], replacing positively and negatively charged ions should approximately correspond to a coordination ratio 8:4 = 2 and should be twice larger for oxygen sublattice. Moreover, the charge of the U4+ ions can further change to U5+. Allen et al.[24] suggested that during the formation of hyperstoichiometric UO_{2+x} the extra oxygen atoms may locate in the interstitial lattice sites forming dumbells along

https://doi.org/10.1557/jmr.2015.261 Published online by Cambridge University Press

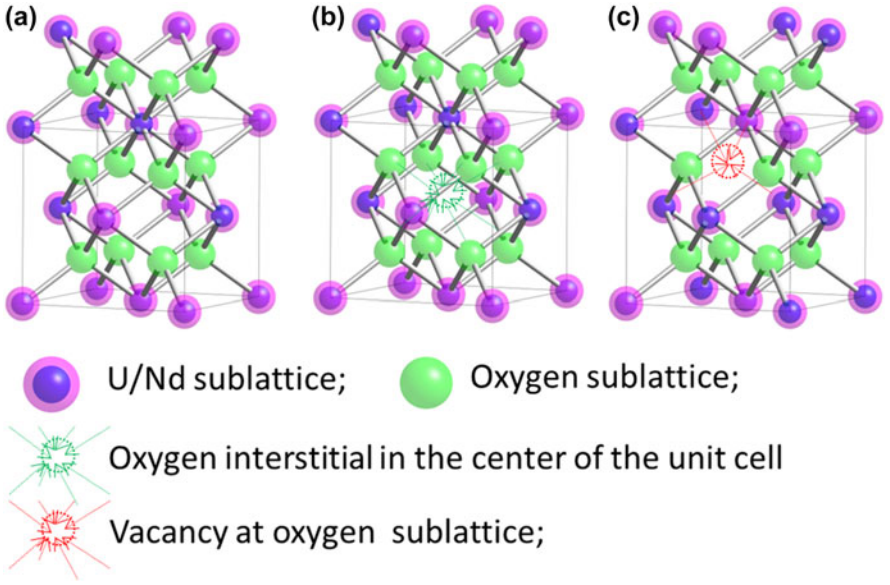


FIG. 11. Structure of the $U_{1-y}Nd_yO_{2.00-x}$ unit cell: (a) $UNdO_2$ unit cell; (b) vacancy at the U/Nd sublattice; (c) vacancy at the oxygen sublattice. Vacancy is shown with red dashed circle.

⟨110⟩ and ⟨111⟩ directions and accompanied by the formation of two vacancies. According to Ohmichi et al.[13] "a U^{4+} ions substitute U^{5+} ions in holding the eight-coordination for cations". Middleburgh et al.[5] stated that oxygen/vacancy clusters should form in stoichiometric and hypostoichiometric alloys while U^{5+} based cluster may dominate in hyperstoichiometric alloys until all extra interstitial oxygen atoms are exhausted. Park and Olander[48] suggested a defect model for UO_2 that incorporates defect clusters (such as Willis defects[49] and vacancy dimmers). Geng et al.[50] performed a comprehensive investigation of clustering in nonstoichiometric $UO_{2\pm x}$. They specifically modeled the 2:2:2 Willis[49] clusters and showed a "unified way to understand the structure of Willis type clusters in $UO_{2\pm x}$".[51] Hutchings[30] came up with a model of the clusters based on the Frenkel pair with the vacancies located along the diagonal of the cluster. He considered the formation of Frenkel pairs at high temperatures and discussed the possibility of clusters formed by a combination of vacancies, interstitials, and relaxed ions in the ratio of 3:1:2 or 9:1:8.[30] Ions surrounding the vacancy are pulled closer to the center of the vacancy, locally decreasing the crystal volume ($\Delta V < 0$) due to relaxation of the lattice caused by static displacements of the ions [Figs. 11(b) and 11(c)] and resulting in the negative average deformation of the lattice $\overline{u_{ij}}$ causing a shift of the XRD peaks. Vacancy formation-induced lattice relaxation affects both average unit cell size (measured by XRD), and the total volume of the crystal V. The total volume of the crystal will change by $Nc_v\Delta V_v$, where c_v is the vacancy concentration; N is the total number of lattice sites in the corresponding sublattice; ΔV_v is the volume relaxation due to a single vacancy and is different for the U/Nd and for the oxygen sublattices. If the number of lattice sites does not change during oxygen adjustment, the vacancy concentration introduced by this adjustment can be estimated as $-\delta v/v = c_v$ and, for example, it is equal ~0.18% for groups A, B, C when oxygen concentration increases from 2.0 to 2.08. For the D group samples, the vacancy concentration decreases by ~0.15% when the oxygen concentration is adjusted from 2.0 to 1.9. This number does not include the equilibrium number of vacancies, which are always present in the thermodynamically stable concentration.[41,42] Furthermore, vacancies can cluster and form bubbles, which can further impact the behavior of the fuel.[52] Molecular dynamics simulations[18,52,53] show that the formation of such bubbles near grain boundaries can play an important role during the fission gas release in light water reactors.[54]

E. Nd–UO_2 energetics from atomistic simulations

We have used atomistic modeling to further understand the effect of Nd addition and oxygen vacancies on the lattice parameter. The calculations were performed using the large-scale atomic/molecular massively parallel simulator code.[55] The interatomic pair potentials were taken from Pirzada et al.[56] and Hanken et al.[57] We used a fluorite-structure 2 × 2 × 2 supercell containing 96 atoms for these calculations. The long-range electrostatic interactions were evaluated using Ewald summation. Periodic boundary conditions were applied in all directions, and the lattice parameter obtained for pure UO_2 was 5.46 Å.

The increase in volume with the addition of Nd is expected due to the larger atomic size of Nd compared to U. The calculations show that there is a binding energy of

https://doi.org/10.1557/jmr.2015.261 Published online by Cambridge University Press

0.58 eV between the Nd atoms and the oxygen vacancy indicating their preference to sit next to each other.

Keeping in view the volume dependence shown in Fig. 10, the addition of Nd^{3+} to UO_2 and oxygen off-stoichiometry can be elucidated from simulations. Nd^{3+} addition can be mediated by two possible defect reactions, i.e., (i) by oxygen vacancy formation mechanism and (ii) via U^{5+} charge compensation mechanism. In both mechanisms, point defects aggregate to form charge-neutral clusters, i.e., $\left(V_O^{\cdot\cdot} : 2Nd_U^t\right)^X$ and $2\left(U_U^{\cdot} : Nd_U^t\right)^X$, respectively. The two reactions leading to the clusters are represented via Kröger–Vink notation shown in the following equations.

$$Nd_2O_3 + O_O^X + 2U_U^X \rightarrow \left(V_O^{\cdot\cdot} : 2Nd_U^t\right)^X + 2UO_2 \quad , \quad (1)$$

$$Nd_2O_3 + O_t'' + 2U_U^{\cdot} \rightarrow \left(U_U^{\cdot} : Nd_U^t\right) + 2UO_2 \quad . \quad (2)$$

Figure 12 shows the volume change due to point defects calculated via atomistic simulations. We find that an individual oxygen vacancy (1 Ovac in Fig. 13) leads to volume contraction, whereas an Nd atom leads to an apparent volume expansion (1 Nd). The oxygen volume contraction is consistent with previous ab intio calculations.[58] The volume expansion from the addition of individual Nd atoms is due to the larger atomic radius. When point defects are clustered together, the volume change via the two mechanisms have opposite effects, i.e., $2\left(U_U^{\cdot} : Nd_U^t\right)$ cluster via vacancy mechanism leading to a volume expansion; $2\left(U_U^{\cdot} : Nd_U^t\right)$ cluster via a U^{5+} charge compensation mechanism leading to a volume contraction. This result is consistent with previous studies[5,6] and illustrates that the U^{5+} charge compensation mechanism may also be responsible for the volume contraction observed in Fig. 7.

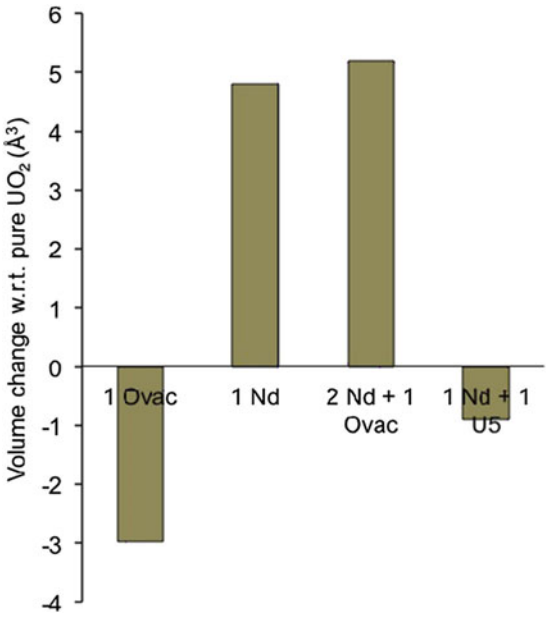


FIG. 12. Volume change with respect to pure UO_2 due to (1) individual oxygen vacancy, (2) individual Nd atom at uranium site, (3) charge neutral cluster containing 2 Nd^{3+} + 1 oxygen vacancy, and (4) charge neutral cluster containing 1 Nd^{3+} and 1 U^{5+}. The volume contraction observed experimentally is due to the formation of $\left(U_U^{\cdot} : Nd_U^t\right)$ cluster.

Figure 12 also shows that increasing oxygen concentration in the hyperstoichiometric region further decreases lattice volume. This volume decrease due to addition of oxygen atoms has been previously studied by Andersson et al.[59] Using ab initio calculations, they showed that this volume decrease is due to formation of different phases, i.e., U_4O_9, U_3O_7, U_3O_8, and reaches the minimum volume at U_2O_5 phase. Thus, the experimental results in Fig. 10 on the hyperstoichiometric systems are also in agreement with simulations.

F. Rietveld refinement of high energy XRD and PDF analysis for O/M = 2

The comparison of the HRXRD patterns collected for the four O/M = 2 samples is shown in Figs. 5 and 13. The HRXRD patterns show several changes with increasing Nd content. These include an increase in the background and decrease in amplitude of the UO_2 peaks with increasing Two Theta. No other characteristic peaks from secondary phases can be identified in the observed patterns, although the peaks for the 29.5 and 53.0 % Nd samples shown considerable line broadening and change in peak heights as shown from the profile fitting results in Fig. 13. Like the laboratory results, the synchrotron measurements for the high Nd concentration samples indicate that increasing Nd concentration promotes an increase in the vacancy concentration and potentially the formation of small clusters with increasing Nd concentration. The two component Rietveld refinements are shown in Fig. 13 and the quantitative results are given in Table II. Several trends in the site occupancy, consistent with discussion above can be seen in these results. These include the occupancy of the O atoms steadily decreasing while the refined Nd fraction increases with increasing Nd concentration, indicating that Nd does indeed promote the formation of O vacancies.

The small refined fractions of the nanophase in the A–C samples also indicate that clustering is only very minor in these samples. Sample D, however, shows the largest nanocomponent with UNdO clusters of ~41 nm in size. We note that the Nd and U occupancies retuned from the Rietveld analysis are potentially correlated, and the ambiguity in the comparison between the nominal refined and fabrication values may thus be due to the limited resolution of the experimental set-up. HRXRD analysis may be of interest in the future to ascertain the U and Nd occupancies.

https://doi.org/10.1557/jmr.2015.261 Published online by Cambridge University Press

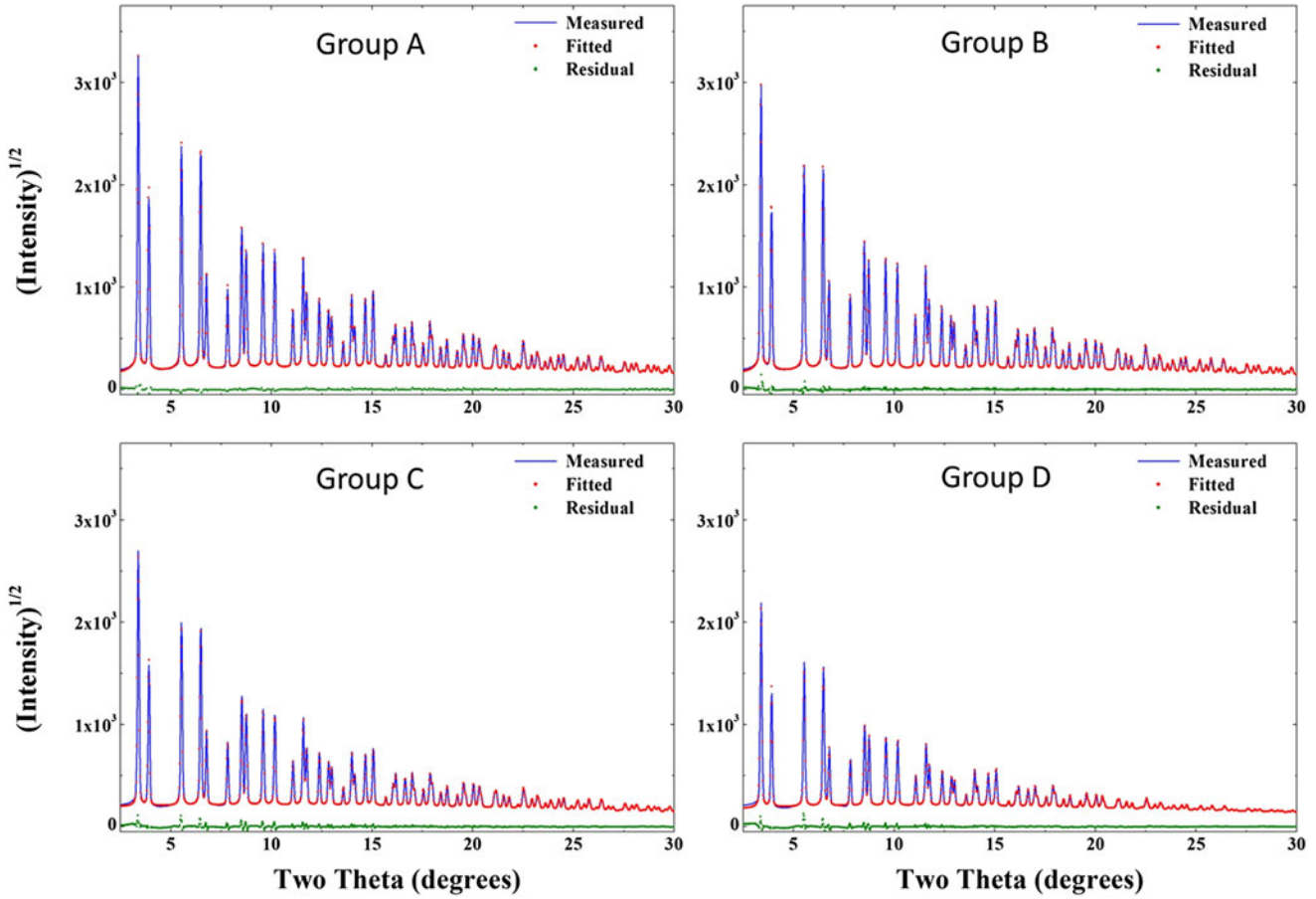


FIG. 13. Measured HRXRD (solid blue line) and Rietveld refined (red marker) for samples with oxygen concentration equal to 2.0.

TABLE II. Synchrotron XRD Rietveld refinement results for the samples prepared with oxygen concentrations equal to 2.0.

Sample	Phase	Weight (%)	*a* (Å)	Occupancy	Size (nm)	Rwp (%)
A	Matrix	95.4 (0.9)	5.456 (0.001)	U: 0.89 (0.01) Nd: 0.11 (0.01) O: 1.00 (0.02)	. . .	3.0
	Nano	4.6 (0.9)	5.586 (0.022)	U: 0.94 (fixed) Nd: 0.06 (fixed) O: 1.00 (fixed)	1.0 (0.2)	. . .
B	Matrix	95.8 (0.7)	5.460 (0.001)	U: 0.79 (0.01) Nd: 0.21 (0.02) O: 0.98 (0.01)	. . .	3.3
	Nano	4.2 (0.7)	5.583 (0.021)	U: 0.85 (fixed) Nd: 0.16 (fixed) O: 1.00 (fixed)	1.1 (0.2)	. . .
C	Matrix	96.1 (0.5)	5.452 (0.001)	U: 0.60 (0.01) Nd: 0.40 (0.01) O: 0.84 (0.02)	. . .	3.43
	Nano	3.9 (0.5)	5.501 (0.014)	U: 0.71 (fixed) Nd: 0.30 (fixed) O: 1.00 (fixed)	2.1 (0.2)	. . .
D	Matrix	84.28 (0.6)	5.447 (0.001)	U: 0.28 (0.01) Nd: 0.72 (0.02) O: 0.56 (0.01)	. . .	3.42
	Nano	15.72 (0.6)	5.467 (0.001)	U: 0.47 (fixed) Nd: 0.53 (fixed) O: 1.0 (fixed)	40.6 (2.7)	. . .

https://doi.org/10.1557/jmr.2015.261 Published online by Cambridge University Press

Figure 14(a) shows the reduced total scattering structure functions $F(Q)$ for the four samples measured. Dampening of the high-Q component with Nd concentration is observable, (most noticeable in the 29.5 and 53.0 % Nd sample). The large increase in the diffuse-scattering component is indicative that higher Nd concentrations lead to an increase in disorder [compare the amplitude of red and blue lines at Fig. 14(a)]. The resulting PDFs for the four samples are shown in Fig. 14(b). Qualitatively, the structure among all samples appears very similar. Information about bond length and bond angle changes can be further extracted from PDF analysis.[60,61] Moreover, the peak width analysis relates to the correlated atomic displacements.[62] Upon detailed inspection, there appears to be a slight shifting (and/or asymmetry) of the peaks to lower radial distance with higher Nd concentrations. This apparent bond length contraction is consistent with the lattice contraction observed above. The peak widths also broaden with increasing Nd concentration, again revealing a higher disorder in the concentrated solid solutions described with pair and higher order correlations similar to the

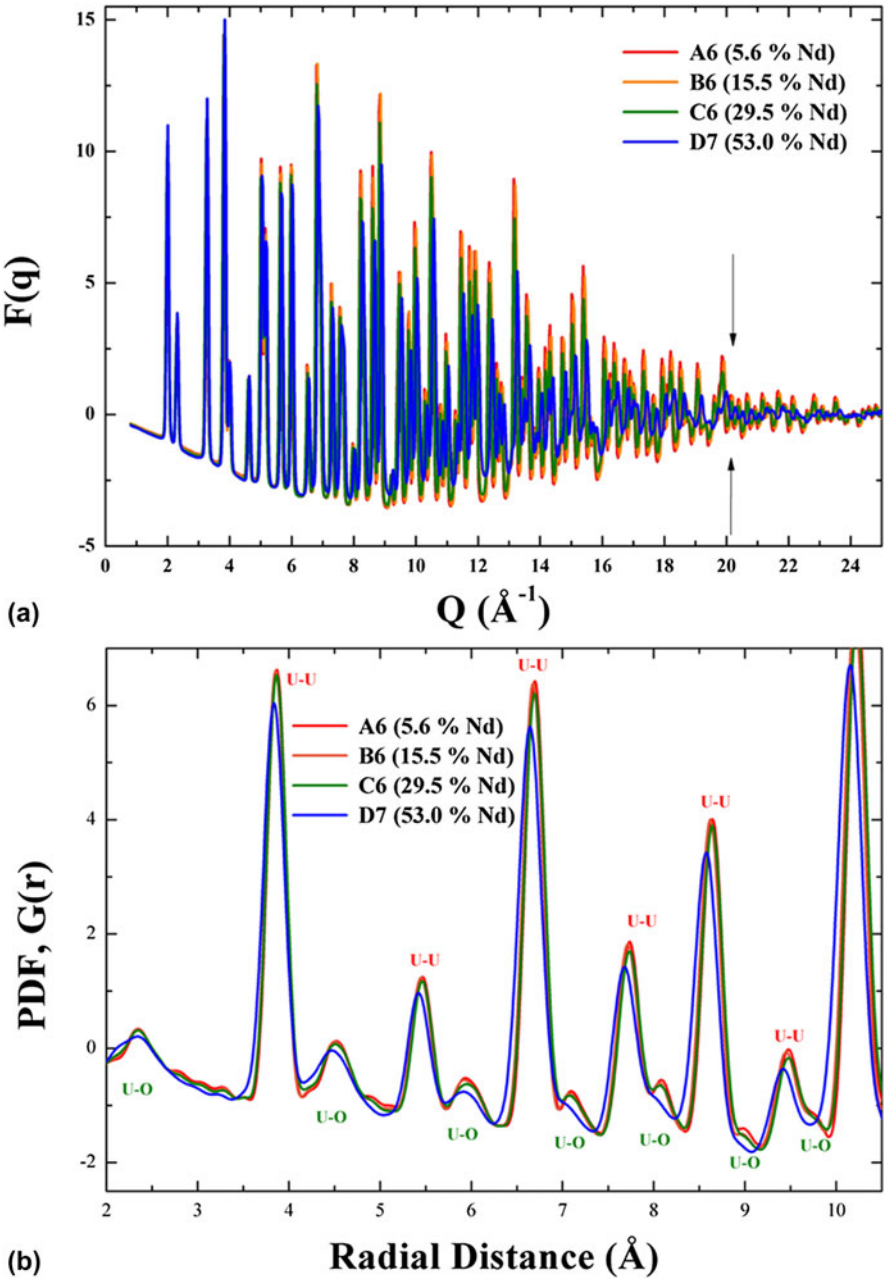


FIG. 14. (a) Reduced structure functions for the UNdO samples; (b) atomic PDF's for the UNdO samples with oxygen concentration equal to 2.0 series. The atomic pairs labeled for reference.

https://doi.org/10.1557/jmr.2015.261 Published online by Cambridge University Press

Ref. 63. Both the peak broadening and shifting of the PDFs could potentially be attributable to the multiple environments quantified from the diffraction analysis above. The combination of the matrix (with contacted unit cell) and the nanophase (that increases with Nd concentration) will both result in U–O and Nd–O bond distances dissimilar to the original undoped local structure.

IV. CONCLUSIONS

The most important findings and conclusions of this study can be summarized as follows:

(1) The lattice parameters and *d*-spacings consistently decrease with Nd concentration.

(2) The lattice parameters and *d*-spacings consistently decrease with oxygen concentration at all Nd concentrations.

(3) The lattice parameter-dependence with Nd concentration for high-concentrations of Nd deviates from the Vegard's law even at oxygen concentration equal 2.0 corresponding to stoichiometric $(U_{1-y}Nd_y)O_2$ compositions.

(4) An increase in the initial holding time improves the homogeneity of Nd cations distribution across the pellet.

(5) At high Nd concentrations, the formation of a nanocrystalline $(U_{1-y}Nd_y)O_2$ component is observed.

(6) The positive binding energy between Nd and oxygen vacancy as well as the formation of U^{5+} charge compensation lead to a contraction in the lattice parameter, as observed experimentally. Therefore, both a U^{5+} charge compensation mechanism together with vacancy formation is responsible for the observed volume contraction.

ACKNOWLEDGMENTS

Research is sponsored by the Department of Energy Office of Nuclear Energy, Fuel Cycle Research and Development Program. The calculations (DSA) were supported by the U.S. Department of Energy, Office of Science, Basic Energy Sciences, Materials Sciences and Engineering Division. The National Synchrotron Light Source at Brookhaven National Laboratory is supported under U.S.D.O.E. Grant No. DE-AC02-98CH10886.

REFERENCES

1. A.M. Fedosseev, M.S. Grigoriev, N.A. Budantseva, D. Guillaumont, C. Le Naour, E. Simoni, C. Den Auwer, and P. Moisy: Americium(III) coordination chemistry: An unexplored diversity of structure and bonding. *C. R. Chim.* **13**(6–7), 839 (2010).
2. W.J. Weber, R.C. Ewing, C.R.A. Catlow, T. Diaz de la Rubia, L.W. Hobbs, C. Kinoshita, Hj. Matzke, A.T. Motta, M. Nastasi, E.K.H. Salje, E.R. Vance, and S.J. Zinkle: Radiation effects in crystalline ceramics for the immobilization of high-level nuclear waste and plutonium. *J. Mater. Res.* **13**(6), 1434 (1998).
3. V. Cocalia, K. Gutowski, and R. Rogers: The coordination chemistry of actinides in ionic liquids: A review of experiment and simulation. *Coord. Chem. Rev.* **250**(7–8), 755 (2006).
4. Z. Szabo, T. Toraishi, V. Vallet, and I. Grenthe: Solution coordination chemistry of actinides: Thermodynamics, structure and reaction mechanisms. *Coord. Chem. Rev.* **250**(7–8), 784 (2006).
5. S.C. Middleburgh, R.W. Grimes, K.H. Desai, P.R. Blair, L. Hallstadius, K. Backman, and P. Van Uffelen: Swelling due to fission products and additives dissolved within the uranium dioxide lattice. *J. Nucl. Mater.* **427**(1–3), 359 (2012).
6. S.C. Middleburgh, D.C. Parfitt, R.W. Grimes, B. Dorado, M. Bertolus, P.R. Blair, L. Hallstadius, and K. Backman: Solution of trivalent cations into uranium dioxide. *J. Nucl. Mater.* **420**, 268 (2012).
7. K.E. Sickafus, R.W. Grimes, J.A. Valdez, A. Cleave, M. Tang, M. Ishimaru, S.M. Corish, C.R. Stanek, and B.P. Uberuaga: Radiation-induced amorphization resistance and radiation tolerance in structurally related oxides. *Nat. Mater.* **6**(3), 217 (2007).
8. M. Denecke: Actinide speciation using X-ray absorption fine structure spectroscopy. *Coord. Chem. Rev.* **250**(7–8), 730 (2006).
9. C. Fillaux, C. Den Auwer, D. Guillaumont, D.K. Shuh, and T. Tyliszczak: Investigation of actinide compounds by coupling X-ray absorption spectroscopy and quantum chemistry. *J. Alloys Compd.* **444–445**, 443 (2007).
10. C. Fillaux, J-C. Berthet, S.D. Conradson, P. Guilbaud, D. Guillaumont, C. Hennig, P. Moisy, J. Roques, E. Simoni, D.K. Shuh, T. Tyliszczak, I. Castro-Rodriguez, and C. Den Auwer: Combining theoretical chemistry and XANES multi-edge experiments to probe actinide valence states. *C. R. Chim.* **10**(10–11), 859 (2007).
11. K.N. Raymond, D.L. Wellman, C. Sgarlata, and A.P. Hill: Curvature of the lanthanide contraction: An explanation. *C. R. Chim.* **13**(6–7), 849 (2010).
12. H. Xue, R. Verma, and J-M. Shreeve: Review of ionic liquids with fluorine-containing anions. *J. Fluorine Chem.* **127**(2), 159 (2006).
13. T. Ohmichi, S. Fukushima, A. Maeda, and H. Watanabe: On the relation between lattice parameter and O/M ratio for uranium dioxide-trivalent rare earth oxide solid solution. *J. Nucl. Mater.* **102**, 40 (1981).
14. H.W. Goldstein, E.F. Neilson, P.N. Walsh, and D. White: The heat capacities of yttrium oxide (Y_2O_3), lanthanum oxide (La_2O_3), and neodymium oxide (Nd_2O_3) from 16 to 300 degrees K. *J. Phys. Chem.* **63** 1445, (1959).
15. O.S. Vălu, D. Staicu, O. Beneš, R.J.M. Konings, and P. Lajarge: Heat capacity, thermal conductivity and thermal diffusivity of uranium–americium mixed oxides. *J. Alloys Compd. V* **614**, 144 (2014).
16. M.I. Lelet, E.V. Suleimanov, A.V. Golubev, C.A. Geiger, W. Depmeier, D. Bosbach, and E.V. Alekseev: Thermodynamic properties and behaviour of A2[(UO2)(MoO4)2] compounds with A=Li, Na, K, Rb, and Cs. *J. Chem. Thermodyn.* **79**, 205 (2014).
17. B.A. Mamedov: Accurate analytical evaluation of heat capacity of nuclear fuels using Einstein-Debye approximation. *Nucl. Eng. Des.* **276**, 124 (2014).
18. Y.F. Zhang, P.C. Millett, M.R. Tonks, X.M. Bai, and S.B. Biner: Molecular dynamics simulations of intergranular fracture in UO_2 with nine empirical interatomic potentials. *J. Nucl. Mater.* **452**(1–3), 296 (2014).
19. C. Guéneau, N. Dupin, B. Sundman, C. Martial, J-C. Dumas, S. Gossé, S. Chatain, F. De Bruycker, D. Manara, and R.J.M. Konings: Thermodynamic modelling of advanced oxide and carbide nuclear fuels: Description of the U–Pu–O–C systems. *J. Nucl. Mater.* **419**(1–3), 145 (2011).

https://doi.org/10.1557/jmr.2015.261 Published online by Cambridge University Press

20. A.G. Matveeva, M.S. Grigoriev, T.K. Dvoryanchikova, S.V. Matveev, A.M. Safiulina, O.A. Sinegribova, M.P. Passechnik, I.A. Godovikov, D.A. Tatarinov, V.F. Mironov, and I.G. Tananaev: Complexes of (2-methyl-4-oxopent-2-yl)diphenylphosphine oxide with uranyl and neodymium nitrates: Synthesis and structures in the solid state and in solution. *Russ. Chem. Bull.* **61**(2), 399 (2012).
21. J.W. McMurray, D. Shin, B.W. Slone, and T.M. Besmann: Thermodynamic reassessment of U-Gd-O system. *J. Nucl. Mater.* **452**(1–3), 397 (2014).
22. W. Huang and H. Chen: Investigation of the elastic, hardness, and thermodynamic properties of actinide oxides. *Phys. B: Condens. Matter* **449**, 133 (2014).
23. Y.N. Hou, X.T. Xu, N. Xing, F.Y. Bai, S.B. Duan, Q. Sun, S.Y. Wei, Z. Shi, H.Z. Zhang, and Y.H. Xing: Photocatalytic application of 4f-5f inorganic-organic frameworks: Influence of Lanthanide contraction on the structure and functional properties of a series of uranyl-lanthanide complexes. *Chempluschem* **79**(9), 1304 (2014).
24. G.C. Allen, P.A. Tempest, and J.W. Tyler: Coordination model for the defect structure of hyperstoichiometric UO_{2+x} and U_4O_9. *Nature* **295**, 48 (1982).
25. L. Desgranges, Y. Pontillon, P. Matheron, M. Marcet, P. Simon, G. Guimbretiere, and F. Porcher: Miscibility gap in the U-Nd-O phase diagram: A new approach of nuclear oxides in the environment? *Inorg. Chem.* **51**(17), 9147 (2012).
26. S-M. Lee, T.W. Knigt, S.L. Voit, and R.I. Barabash: The lattice parameter behavior with different Nd and O Concentration in the $(U_{1-y}Nd_y)O_{2\pm x}$ solid solution. *Nucl. Technol.* (2015, in press).
27. A. Albinati, M.J. Cooper, K.D. Rouse, M.W. Thomas, and B.T.M. Willis: Temperature dependence of the atomic thermal displacements in UO_2: A test case for the rietveld profile-refinement procedure. *Acta Crystallogr. A* **A36**, 265 (1980).
28. E.J. Mittemeijer and U. Welzel: The "state of the art" of the diffraction analysis of crystallite size and lattice strain. *Z. Kristallogr.* **223**, 552 (2008).
29. S. Brandstetter, P.M. Derlet, S. Van Petegem, and H. Van Swygenhoven: Williamson–Hall anisotropy in nanocrystalline metals: X-ray diffraction experiments and atomistic simulations. *Acta Mater.* **56**, 165 (2008).
30. M.T. Hutchings: High-temperature studies of UO_2 and ThO_2 using neutron scattering techniques. *J. Chem. Soc. Faraday Trans.* **83**, 1083 (1987).
31. V.F. Hund and U. Peetz: Untersuchungen der Systeme La_2O_3, Nd_2O_3, Sm_2O_3, Yb_2O_3, Sc_2O_3 rnit UsO_8. *Zeitschrift für Anorgariischc Urtd Allgrmeine Chemie* **271**, 6 (1952).
32. M.A. Krivoglaz: *Diffuse Scattering of X-rays and Neutrons by Fluctuations* (Springer, New York, USA, 1996); pp. 284.
33. P.H. Dederichs: The theory of diffuse x ray scattering and its application to the study of point defects and their clusters. *J. Phys. F: Metal Phys.* **3**, 471 (1973).
34. R.I. Barabash, G.E. Ice, E.A. Karapetrova, and P. Zschack: Stress annealing induced diffuse scattering from Ni_3 (Al, Si) precipitates. *Metall. Mater. Trans. A.* **43**(5), 1413 (2011).
35. R.I. Barabash, J.S. Chung, and M.F. Thorpe: Lattice and continuum theories of Huang scattering. *J. Phys.: Condens. Matter* **11**, 3075 (1999).
36. R.E. Stoller, F.J. Walker, E.D. Specht, D.M. Nicholson, R.I. Barabash, P. Zschack, and G.E. Ice: Diffuse X-ray scattering measurements of point defects and clusters in iron. *J. Nucl. Mater.* **367–370**, 269 (2007).
37. R.I. Barabash and M.A. Krivoglaz: Influence of anisotropy on X-ray scattering by highly distorted ageing solid solutions. *Phys. Met. Metall.* **51**(5), 1 (1981).
38. R.I. Barabash and M.A. Krivoglaz: X-ray scattering by polycrystals containing defects with Coulomb displacement fields. *Phys. Met. Metall.* **45**(1), 1 (1979).
39. G.E. Ice, R.I. Barabash, and W-J. Liu: Diffuse X-ray scattering from tiny sample volumes. *Z. Kristallogr.* **220**(12), 1076 (2005).
40. International Center for Diffraction Data (ICDD)\Pair Distribution Functions (PDF)4 + hsrdb. (2012).
41. J.P. Stark: Thermodynamic stability of vacancy concentrations during thermal diffusion experiments. *Scr. Metall. Mater.* **6**, 91 (1972).
42. M.A. Krivoglaz: *X-ray and Neutron Diffraction in Nonideal Crystals* (Springer, New York, USA, 1996); pp. 465.
43. R.D. Shannon: Revised effective ionic radii and systematic studies of interatomic distances in Halides and Chalcogenides. *Acta Crystallogr. Sec. A* **32**, 751 (1976).
44. Y. Yun and W.W. Kim: First principle studies on electronic and defect structures of UO_2, ThO_2, and PuO_2. In *Transactions of Korean Nuclear Society Spring Meeting, Jeju, Korea*, (2007).
45. A. Schwartz, M. Dressel, B. Alavi, A. Blank, S. Dubois, G. Grüner, B. Gorshunov, A. Volkov, G. Kozlov, S. Thieme, L. Degiorgi, and F. Lévy: Fluctuation effects on the electrodynamics of quasi-one-dimensional conductors above the charge-density-wave transition. *Phys. Rev. B* **52**(8), 5643 (1995).
46. M. Rice and E. Mele: Possibility of solitons with charge $\pm$e/2 in highly correlated 1:2 salts of tetracyanoquinodimethane (TCNQ). *Phys. Rev. B* **25**(2), 1339 (1982).
47. J. Pang, W. Buyers, A. Chernatynskiy, M. Lumsden, B. Larson, and S. Phillpot: Phonon lifetime investigation of anharmonicity and thermal conductivity of UO_2 by neutron scattering and theory. *Phys. Rev. Lett.* **110**, 15 (2013).
48. K. Park and D.R. Olander: A defect model for the oxygen potential of urania. *High Temp. Sci.* **29**, 203 (1990).
49. B.T.M. Willis: The defect structure of hyper-stoichiometric uranium dioxide. *Acta Crystallogr. A* **34**, 88 (1978).
50. H.Y. Geng, Y. Chen, Y. Kaneta, M. Iwasawa, T. Ohnuma, and M. Kinoshita: Point defects and clustering in uranium dioxide by LSDA+U calculations. arXiv:0806.1790v1 [cond-mat.mtr]-sci] *Rev. B* **77**, 104120 (2008).
51. P. Chakraborty, M.R. Tonks, and G. Pastore: Modeling the influence of bubble pressure on grain boundary separation and fission gas release. *J. Nucl. Mater.* **452**(1–3), 95 (2014).
52. T. Chen, D. Chen, B.H. Sencer, and L. Shao: Molecular dynamics simulations of grain boundary thermal resistance in UO_2. *J. Nucl. Mater.* **452**(1–3), 364 (2014).
53. J. Rest and S.M. Gehl: The mechanistic prediction of transient fission-gas release from LWR fuel. *Nucl. Eng. Des.* **56**(1), 233 (1980).
54. R.J. White and M.O. Tucker: A new fission-gas release model. *J. Nucl. Mater.* **118**(1), 1 (1983).
55. S. Plimpton: Fast parallel algorithms for short-range molecular dynamics. *J. Comput. Phys.* **117**, 1 (1995).
56. M. Pirzada, R.W. Grimes, L. Minervini, J.F. Maguire, and K.E. Sickafus: Oxygen migration in $A_2B_2O_7$ pyrochlores. *Solid State Ionics* **140**, 201 (2001).
57. B.E. Hanken, C.R. Stanek, N. Gronbech-Jensen, and M. Asta: Computational study of the energetics of charge and cation mixing in $U_{(1-x)}Ce_{(x)}O_2$. *Phys. Rev. B* **84**, 085131 (2011).
58. D.S. Aidhy, B. Liu, Y. Zhang, and W.J. Weber: Chemical expansion affected oxygen vacancy stability in different oxide structures from first principles calculations. *Comput. Mater. Sci.* **99**, 298 (2015).
59. D.A. Andersson, G. Baldinozzi, L. Desgranges, D.R. Conradson, and S.D. Conradson: Density functional theory calculations of UO_2 oxidation: Evolution of UO_{2+x}, U_4O_{9-y}, U_3O_7 and U_3O_8. *Inorg. Chem.* **52**, 2769 (2013).
60. Th. Proffen and S.J.L. Billinge: PDFFIT, a program for full profile structural refinement of the atomic pair distribution function. *J Appl Cryst.* **32**, 572 (1999).
61. J. Perdew and Y. Wang: Pair-distribution function and its coupling-constant average for the spin-polarized electron gas. *Phys. Rev. B. Condens. Matter.* **46**(20), 12947 (1992).

https://doi.org/10.1557/jmr.2015.261 Published online by Cambridge University Press

62. Th. Proffen, S.J.L. Billinge, T. Egami, and D. Louca: Structural analysis of complex materials using the atomic pair distribution function – A practical guide. *Z. Kristallogr.* **218**, 132 (2003).

63. D.M.C. Nicholson, R.I. Barabash, G.E. Ice, C.J. Sparks, J. Lee Robertson, and C. Wolverton: Relationship between pair and higher-order correlations in solid solutions and other Ising systems. *J. Phys.: Condens. Matter* **18**(50), 11585 (2006).

https://doi.org/10.1557/jmr.2015.261 Published online by Cambridge University Press